A new analytical model to predict the formation of necking instabilities in porous plates subjected to dynamic biaxial loading

M. Anil Kumar, K. E. N'souglo*, J. A. Rodríguez-Martínez

Department of Continuum Mechanics and Structural Analysis. University Carlos III of Madrid. Avda. de la Universidad, 30. 28911 Leganés, Madrid, Spain

Abstract

In this paper, we have developed a linear stability analysis to predict the formation of necking instabilities in porous ductile plates subjected to dynamic biaxial stretching. The mechanical behavior of the material is described with the Gurson-Tvergaard-Needleman constitutive relation for progressively cavitating solids (Gurson, 1977; Tvergaard, 1981, 1982; Tvergaard and Needleman, 1984) which considers the voids to be spherical and the matrix material isotropic with yielding defined by the von Mises (1928) criterion. The analytical model is formulated in a two-dimensional framework in which the multiaxial stress state that develops inside the necked region is approximated with the Bridgman (1952) correction factor, superimposing a hydrostatic stress state to the uniform stress field that develops in the plate before localization. As opposed to the linear stability models published so far to model dynamic necking in ductile plates, which consider the material to be fully dense and incompressible, the approach developed in this paper provides new insights into the interplay between porosity and inertia on plastic localization. In addition, the predictions of the theoretical model for the critical strain leading to necking formation have been compared with unit-cell finite element calculations performed in ABAQUS/Explicit (2019). Satisfactory quantitative and qualitative agreement has been found between the theoretical and computational approach for loading paths ranging from plane strain tension to nearly equibiaxial tension, loading rates varying from 100 s^{-1} to 10000 s^{-1}, and different values of the initial void volume fraction ranging from 0.01 to 0.1. Both analytical and finite element results suggest that the influence of porosity on necking localization increases, due to early voids coalescence, as the loading rate increases and the loading path approaches equibiaxial tension. The original formulation developed in this paper serves as a basis for analytically modeling the dynamic formability of porous ductile plates, and it can be readily extended to consider more complex porous plasticity theories, e.g. constitutive models which consider the anisotropy of the material (Benzerga and Besson, 2001) and/or voids with different shapes (Gologanu et al., 1993; Monchiet et al., 2008).

Keywords:

*Corresponding author. E-mail address: knsouglo@ing.uc3m.es

Dynamic formability, Porous plasticity, Linear stability analysis, Necking instabilities

1. Introduction

Linear stability theories have been widely accepted as an effective approach for identifying the mechanisms which control necking localization in metallic materials subjected to dynamic loading. This technique is based on the superposition of a small perturbation on the homogeneous solution of the problem considered, so that if the perturbation grows faster than the background solution, the plastic flow is unstable and a non-homogeneous, neck-like deformation field can develop.

Chou and Carleone (1977) formulated a one-dimensional perturbation analysis to investigate the stability of plastic shaped-charge jets subjected to dynamic loading and thus provide insights into the mechanisms which control the formation of multiple necks and fragments in the jets at large strains. The jet was modelled as a slender rod with circular cross-section deforming at constant stretch rate. Moreover, the material was considered to be incompressible, rate-independent and with non-linear strain hardening. Consistent with the Considère (1885) criterion, it was shown that the perturbation was stable –i.e. the necking condition was not met– if the stress was smaller than the slope of the stress-strain curve. On the other hand, it was shown that for unstable jets, the smaller the flow stress, and the larger the material density and the stretching rate, the slower the growth rate of the perturbation, and so the development of the necking pattern. Moreover, the one-dimensional analysis did not yield a finite critical wavelength which causes the fastest growth, so that the perturbation growth increased monotonically with the decrease of the perturbation wavelength. Chou and Carleone (1977) pointed out that it is necessary to account for the multiaxial stress state which develops in a necked section to demonstrate the existence of a critical wavelength for which the perturbation growth is the fastest. This critical perturbation wavelength –also referred to as critical necking wavelength– was presumed to determine the average spacing between necks in the multiple localization pattern that forms in the shaped-charge jets. Shortly after, Walsh (1984) extended the stability analysis of Chou and Carleone (1977) considering Bridgman (1952) approximation to model within a one-dimensional framework the stress enhancement that occurs in a necked section. The material was considered to be incompressible with constant yield strength. According to Chou and Carleone (1977) predictions, it was shown that the local hydrostatic stress that develops in the neck slows down the growth of short wavelength perturbations, while inertia refrains the growth of long wavelength perturbations, leading to the promotion of a critical wavelength for which the growth rate of the disturbance is maximum (and thus the mechanical energy required to trigger a neck is minimum). In addition, Walsh (1984) applied dimensional considerations to the perturbed stretching jet and showed that the joint effects of strain rate, material density, flow stress and cross-section radius on the perturbation growth –as earlier identified by Chou and Carleone (1977)– can be collected into a single dimensionless parameter which represents the inertial resistance to motion. A later study of Fressengeas and Molinari (1985) on the stability of slender bars modelled with a thermo-viscoplastic constitutive relation and submitted to uniaxial tension demonstrated that inertia is responsible for the increased ductility that metallic materials generally display at high strain rates (e.g. see Wood (1967) and Hu and Daehn (1996)), while thermal softening was shown to favour early necking formation. Consistently with Walsh (1984) analysis, Fressengeas and Molinari (1985) pointed out that consideration of multiaxial stress effects in the necking zone using Bridgman (1952) correction suppresses short wavelengths and delays plastic localization.

Following the works of Walsh (1984) and Fressengeas and Molinari (1985), one-dimensional stability models with Bridgman (1952) correction for the axial stress –which stand out for their simplicity– have been used by several authors to investigate the effect of different aspects of the mechanical behaviour of ductile metals on necking formation. For instance, Zhou et al. (2006) modelled the material behaviour using von Mises (1928) plasticity with yield stress dependent on strain and strain rate, and showed that the strain rate sensitivity slows down the growth of perturbations, so that the necks grow more slowly, which delays plastic localization. Finite difference simulations of a round bar subjected to constant stretching velocity confirmed the predictions of the stability analysis such that increasing the strain rate sensitivity increased the material ductility. Zaera et al. (2014) and Rodríguez-Martínez et al. (2015) investigated the effect of strain induced martensitic transformation and dynamic recrystallization on the inception of multiple necks in steel and titanium bars subjected to dynamic tensile loading. A key feature of the works of Zaera et al. (2014) and Rodríguez-Martínez et al. (2015) was to incorporate into the one-dimensional stability analysis the thermomechanical coupling due to plastic dissipation and the energy release due to the exothermic character of the microstructural transformations. The theoretical predictions were compared with finite element calculations, which confirmed the stabilizing effect of the martensitic transformation on the flow stress, and the destabilizing effect of the dynamic recrystallization, which favours the formation of early necks. Recently, N'souglo et al. (2018) extended the linear stability analysis of Zhou et al. (2006) to consider materials with yielding described with the porous plasticity criterion developed by Gurson (1977). The theoretical predictions for the evolution of the necking strain with strain rate found reasonable agreement with finite element results of long rods subjected to dynamic stretching at strain rates varying from 1000 s^{-1} to 50000 s^{-1}.

Guduru and Freund (2002) derived a three-dimensional stability analysis for rapidly extending cylindrical rods modelled with the constitutive law developed by Stören and Rice (1975) which considers the material to be incompressible, rate-independent with strain hardening. The results obtained for the critical perturbation wavelength were compared with the average neck spacing (number of necks) obtained in the ring expansion tests performed by Grady and Benson (1983) on 1100-0 aluminum and OFHC copper specimens, and satisfactory agreement was obtained for strain rates of the order of 10^4 s^{-1}. The stability analysis of Guduru and Freund (2002) also predicted that the number of necks and the necking strain increase non-linearly with the applied strain rate, consistently with the experimental data obtained by Altynova et al. (1996) for 6061 aluminum and OFHC copper rings expanded at velocities ranging from 50 to 300 m/s. Shortly after, Mercier and Molinari (2003) formulated a three-dimensional linear stability analysis for a cylindrical bar subjected to dynamic extension. As in Guduru and Freund (2002), the material behaviour was modelled with the constitutive relation of Stören and Rice (1975). Mercier and Molinari (2003) showed that inertia slows down the growth of long wavelength perturbations while multidimensional effects (stress multiaxiality) and strain hardening extinct short wavelength perturbations, so that the critical perturbation wavelength depends on the specimen deformation, with the average neck spacing predicted by the stability analysis decreasing with the increase of the strain hardening and the stretch in the bar.

Linear stability models have also been developed to study the formation of dynamic necks in plates and shells. For instance, Fressengeas and Molinari (1994) extended the analysis performed by Hutchinson et al. (1978) for a plate subjected to plane strain tension to consider inertia effects. A non-linear viscous material was employed in the analysis. Fressengeas and Molinari (1994) showed that viscosity preferentially slows down the growth of short wavelength perturbations –consistent with the results obtained by Zhou et al. (2006) using a 1D-stability analysis, see discussion above– and compared the theoretical predictions for the critical wavelength with the average fragments size obtained in experiments and non-linear numerical simulations reported by Karpp and Simon (1976), so that satisfactory agreement was obtained for copper shaped-charged jets deforming at high strain rates of the order of 8000 s^{-1}. Moreover, Shenoy and Freund (1999) generalized the quasi-static analysis of the plane tension test developed by Hill and Hutchinson (1975) to include dynamic effects. The critical perturbation wavelength was shown to decrease with increasing strain rate, so that the number of necks predicted by the theoretical model increased with the applied loading velocity, in qualitative agreement with the ring expansion experiments of Grady and Benson (1983) and Altynova et al. (1996). Years later, Mercier et al. (2010) developed a linear stability analysis to model necking localization in experiments performed with tantalum and copper hemispherical shells subjected to dynamic expansion at strain rates varying between 10^3 s^{-1} and 10^4 s^{-1}. The motion of the hemispheres was not spherically divergent, resulting in the formation of multiple necking bands parallel to each other in an axisymmetric layer located near the equatorial plane where the material stretched under plane strain conditions. The plane strain model of Mercier et al. (2010) was an extension of earlier formulations developed by Fressengeas and Molinari (1994) and Mercier and Molinari (2003) to consider von Mises materials with flow stress dependent on strain, strain rate and temperature. Based on a so-called effective strain rate sensitivity parameter, which merged the thermal and the visco-plastic material characteristics, Mercier et al. (2010) obtained a criterion to determine using the stability analysis the critical strain leading to necking formation and the average spacing between necks. The theoretical predictions were in agreement with the experiments for both tantalum and copper specimens. Shortly after, Jouve (2013, 2015) formulated three-dimensional stability models to predict the formation of necking instabilities in plates of arbitrary thickness subjected to plane strain tension and biaxial tension, respectively. The mechanical behaviour of the material was modelled with von Mises (1928) plasticity, associated flow rule and flow strength dependent on plastic strain, plastic strain rate and temperature. Adiabatic conditions of deformation were considered. The analysis was performed for moderate strain rates within the range 10 s^{-1} – 20 s^{-1}. Consistent with Fressengeas and Molinari (1994), Jouve (2013, 2015) showed that viscosity essentially refrains the growth of the shortest wavelength instabilities, and identified a loading-path-dependent critical value of material viscosity above which inertia effects on necking formation are negligible (for the range of strain rates considered). Moreover, Zaera et al. (2015) developed a 2D linear stability analysis to model necking formation in thin-plates plates subjected to in-plane biaxial loading for strain rates of the order of 1000 s^{-1}, i.e. above the range of strain rates considered by Jouve (2013, 2015). The model of Zaera et al. (2015) was essentially an extension of earlier formulation of Dudzinski and Molinari (1991) to account for inertia effects, considering Bridgman (1952) correction for the axial stress (in-plane normal stress perpendicular to the necking band). As in Jouve (2013, 2015), the material was modelled with von Mises (1928) plasticity, and a thermo-viscoplastic constitutive relation for the evolution of the yield stress. The predictions of the stability analysis were used to construct forming limit diagrams that were in qualitative agreement with results obtained from finite element calculations, and showed that the critical perturbation wavelength increases as the loading path moves away from uniaxial tension and approaches equibiaxial tension, and so does, therefore, the spacing between necks in the multiple necking patterns predicted in the numerical calculations (see also Rodríguez-Martínez et al. (2017)).

The stability analysis formulation of Zaera et al. (2015) has been later extended to consider different plasticity theories with the aim of studying the effect of various aspects of the mechanical behaviour of ductile metals on dynamic necking localization in thin plates. For instance, N'souglo et al. (2020) employed the isotropic form of the Cazacu et al. (2006) yield criterion, which accounts for the effect of tension-compression asymmetry in flow stresses, and showed that the necking strain is significantly greater for a material that displays a larger flow stress in uniaxial compression than in uniaxial tension. The stability analysis calculations performed for plates subjected to dynamic plane strain tension, at strain rates ranging from 4000 s^{-1} to 80000 s^{-1}, were compared with unit-cell finite element simulations assuming that a perturbation mode turns into a necking mode when a critical value of the perturbation growth rate is met. Satisfactory qualitative and quantitative agreement between stability analysis and finite element results was obtained for all the perturbation wavelengths and strain rates investigated. Moreover, N'souglo et al. (2021) considered plastic orthotropic materials modelled with the yield criterion developed by Hill (1948) and performed the stability analysis for loading paths ranging from plane strain tension to equibiaxial tension, and for strain rates varying between 100 s^{-1} and 50000 s^{-1}. Assuming that a neck is formed when the perturbation growth rate reaches a critical value –as in N'souglo et al. (2020)–, the stability analysis was employed to construct forming limit diagrams that found good correlation with the results obtained from the non-linear two zone model developed by Jacques (2020) and with unit-cell finite element calculations. N'souglo et al. (2021) concluded that the effect of anisotropy on dynamic formability increases as the loading path moves away from plane strain and approaches equibiaxial tension, but it is not significantly affected by the prescribed strain rate. Very recently, Rodríguez-Martínez et al. (2021) developed a linear stability analysis for plates subjected to plane strain tension modelled with the isotropic Drucker (1949) yield criterion, which depends on both the second and third invariant of the stress deviator. The analysis was performed for effective strain rates ranging from 10^{-4} s^{-1} to $8 \cdot 10^4$ s^{-1}, and the theoretical results were compared with uni-cell finite element calculations, as in N'souglo et al. (2020, 2021). Both stability analysis and finite element results showed that for quasi-static loadings the specimen elongation when necking occurs is virtually insensitive to the third invariant of the stress deviator. In contrast, for large values of the prescribed effective strain rate, the influence of the third invariant becomes important, notably for long wavelengths, so that the specimen elongation when necking occurs increases as the ratio between the yield stresses in uniaxial tension and in pure shear increases, while the necking strain decreases.

However, to the authors' knowledge, all the linear stability models developed so far to study the formation of dynamic necks in plates and shells –most of them cited in previous two paragraphs– consider the material to be fully dense and incompressible. As of today, there is no specific formulation for porous materials. In order to fill this gap, in this paper we have developed a two-dimensional perturbation analysis for thin plates modelled with the Gurson-Tvergaard-Needleman constitutive relation (Gurson, 1977; Tvergaard, 1981, 1982; Tvergaard and Needleman, 1984) and subjected to in-plane dynamic loading. The stress multiaxiality effects in the necked region have been approximated using Bridgman (1952) correction. Moreover, we have investigated loading paths ranging from plane strain tension up to equibiaxial tension, and strain rates varying from 100 s^{-1} to 10000 s^{-1}. An original contribution of this work is that we have enhanced the calibration procedure developed by N'souglo et al. (2020) for the stability analysis, so that in this paper a perturbation mode is considered to turn into a necking mode based on a function of the perturbation growth rate which takes into account the combined effect that loading path and loading rate have on the necking strain. The stability analysis predictions obtained with this novel necking criterion have been compared with unit-cell finite element calculations, and satisfactory agreement has been obtained for all the strain rates and loading paths considered. An important outcome of this work is that both analytical and finite element results suggest that the influence of porosity on necking localization increases, due to early voids coalescence, as the loading rate increases and the loading path approaches equibiaxial tension.

2. Analytical model

In this section, we develop a 2D perturbation analysis to model the formation of necking instabilities in porous plates subjected to dynamic biaxial stretching. We consider a thin plate of initial thickness h^0 and edges of initial length L^0 subjected to constant in-plane velocities, V_x and V_y, on opposed sides, see Fig. 1. Cartesian coordinates (X, Y, Z) define the location of a material point in the undeformed state, while the location of the same material point in the deformed configuration is (x, y, z). The origin of both Lagrangian and Eulerian coordinate systems is located at the center of mass of the plate. Note that the out-of-plane direction Z is assumed of plane stress. The elastic strains are neglected, and the mechanical behavior of the plate is described with the porous plasticity constitutive relation developed by Gurson (1977), Tvergaard (1981, 1982) and Tvergaard and Needleman (1984) which accounts for void growth and coalescence. The multiaxial stress state that develops inside a necked region is modeled with Bridgman (1952) approximation superimposing a hydrostatic stress state to the uniform stress field that develops in the plate during homogeneous deformation (before necking localization, see the works of Zhou et al. (2006), Zaera et al. (2015) and Xavier et al. (2021), among others).

2.1. Governing equations

The strain rates in the loading directions are:

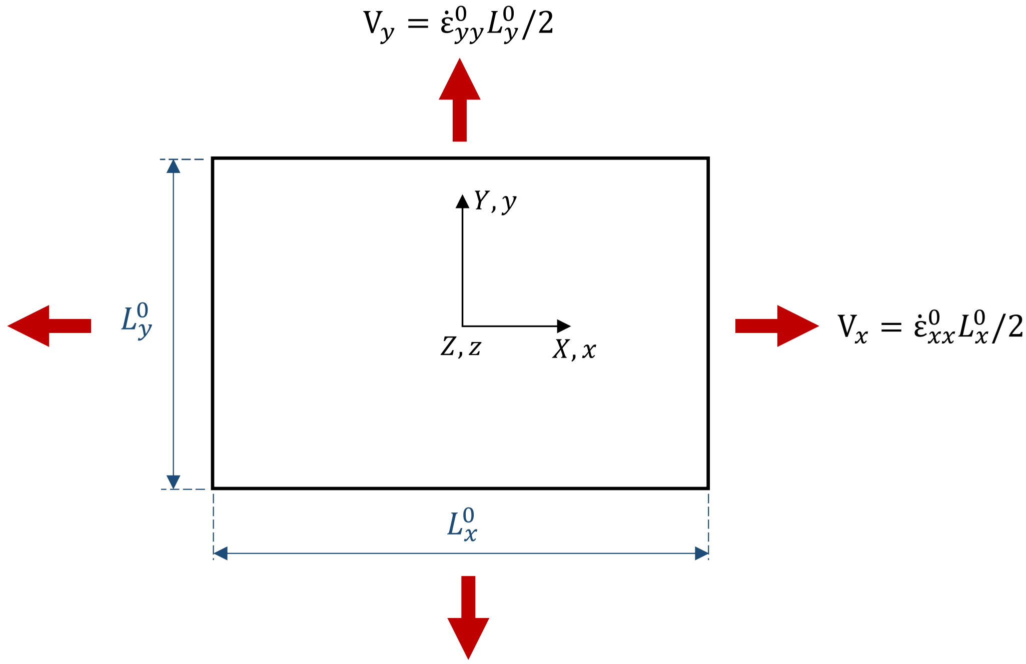

Figure 1: Schematic representation of the geometry and boundary conditions of the problem addressed: a thin plate of initial thickness h^0 and edges of initial length L^0 is subjected to constant and opposed stretching velocities, V_x and V_y, on opposed sides. The Lagrangian and Eulerian Cartesian coordinate systems, (X, Y, Z) and (x, y, z), respectively, with origin located at the center of mass of the plate, are associated to the applied velocity field.

$$\begin{aligned} d_{xx} &= \frac{\partial V_x}{\partial x} \\ d_{yy} &= \frac{\partial V_y}{\partial y} \end{aligned} \tag{1}$$

which are related to the corresponding stretches, F_{xx} and F_{yy}, and stretch rates, $\dot{F}_{xx}$ and $\dot{F}_{yy}$, as:

$$\begin{aligned} F_{xx} &= \frac{\dot{F}_{xx}}{d_{xx}} \\ F_{yy} &= \frac{\dot{F}_{yy}}{d_{yy}} \end{aligned} \tag{2}$$

Moreover, the through-thickness stretch is:

$$F_{zz} = \frac{h}{h^0} \tag{3}$$

where h is the current thickness of the plate.

The balance of mass provides a relationship between the initial void volume fraction f^0, the current void volume fraction f, and the stretches:

$$F_{xx}F_{yy}F_{zz} = \frac{1-f^0}{1-f} \tag{4}$$

which leads to the following expression for the density ratio:

$$\frac{\rho}{\rho^0} = \left(\frac{1-f}{1-f^0}\right) \tag{5}$$

where ρ and ρ^0 are the current and initial material densities.

The Gurson-Tvergaard-Needleman flow potential is expressed as follows (Gurson, 1977; Tvergaard, 1981, 1982; Tvergaard and Needleman, 1984):

$$\Phi = \left(\frac{\sigma_{xx}^2 + \sigma_{yy}^2 - \sigma_{xx}\sigma_{yy}}{\bar{\sigma}^2}\right) + 2q_1 f^* \cosh\left(\frac{q_2(\sigma_{xx}^{avg} + \sigma_{yy}^{avg} + \sigma_{zz}^{avg})}{2\bar{\sigma}}\right) - 1 - (q_1 f^*)^2 = 0 \tag{6}$$

with q_1 and q_2 being material parameters, $\bar{\sigma}$ the flow strength of the matrix material (see equation (11)), and f^* the effective porosity, defined as:

$$f^* = \begin{cases} f & \text{if} \quad f < f_c \\ f_c + \dfrac{(f_u - f_c)(f - f_c)}{(f_f - f_c)} & \text{if} \quad f_c \leqslant f \leqslant f_f \\ f_u & \text{if} \quad f > f_f \end{cases} \tag{7}$$

where f_c is the void volume fraction at which voids coalesce, f_f is the void volume fraction at final fracture of the material and $f_u = 1/q_1$ is the ultimate void volume fraction.

Moreover, σ_{xx} and σ_{yy} are the uniform stresses in the loading directions (stress field before necking localization), while σ_{xx}^{avg}, σ_{yy}^{avg} and σ_{zz}^{avg} are the average stresses defined as:

$$
\begin{aligned}
\sigma_{xx}^{avg} &= \sigma_{xx} + \sigma_h = B(\varphi)\,\sigma_{xx} \\
\sigma_{yy}^{avg} &= \sigma_{yy} + \sigma_h = \sigma_{yy} + \sigma_{xx}^{avg} - \sigma_{xx} \\
\sigma_{zz}^{avg} &= \sigma_h = \sigma_{xx}^{avg} - \sigma_{xx}
\end{aligned}
\tag{8}
$$

where σ_h denotes the hydrostatic stress that develops in a necked section and $B(\varphi)$ is the correction factor introduced by Bridgman (1952):

$$
B(\varphi) = \sqrt{1+\varphi^{-1}}\ln\left(1+2\varphi+2\sqrt{\varphi(1+\varphi)}\right) - 1 \tag{9}
$$

with:

$$
\varphi = \frac{h}{8}\frac{\partial^2 h}{\partial x^2} \tag{10}
$$

While Bridgman (1952) correction for necking was developed for elastic-perfectly plastic materials under quasi-static loading conditions, in this work we assume that it can be used to approximate the axial stress in the necked section of porous materials with flow strength dependent on strain and strain rate. Moreover, in future works, we shall consider including in the linear stability analysis the one-dimensional model recently developed by Audoly and Hutchinson (2016, 2019) to determine the stress state inside the neck, and we shall compare the results with the approach used in this paper based on the classical theory of Bridgman (1952).

The flow strength of the matrix material is defined as:

$$
\bar{\sigma} = \sigma^0\left(\varepsilon^0 + \bar{\varepsilon}\right)^n \left(\frac{\dot{\bar{\varepsilon}}}{\dot{\varepsilon}^0}\right)^m \tag{11}
$$

where σ^0, ε^0, n, $\dot{\varepsilon}^0$ and m are material parameters, and $\bar{\varepsilon}$ is the effective plastic strain:

$$\bar{\varepsilon} = \int_0^t \dot{\bar{\varepsilon}}\,(\tau)\,\mathrm{d}\tau \tag{12}$$

with $\dot{\bar{\varepsilon}}$ being the effective plastic strain rate. We are aware that at high strain rates, due to local adiabatic heating, the effect of thermal softening on the mechanical behavior of ductile materials is important. Nevertheless, the main objective of this work is to investigate the effect of material porosity on dynamic necking localization, so that neglecting the temperature sensitivity of the material facilitates the interpretation of results. The reader is referred to Section 6.4 of the recent paper of N'souglo et al. (2021) to obtain insights into the effect of adiabatic heating on necking localization in anisotropic ductile plates subjected to dynamic biaxial loading for loading paths varying from plane strain to equibiaxial tension.

Assuming that the rate of macroscopic plastic work is equal to the rate of equivalent plastic work in the matrix material, it follows that:

$$\sigma_{xx}^{avg} d_{xx} + \sigma_{yy}^{avg} d_{yy} + \sigma_{zz}^{avg} d_{zz} = (1 - f)\,\bar{\sigma}\dot{\bar{\varepsilon}} \tag{13}$$

Moreover, considering an associated plastic flow rule, the following relationships between strain rates and stresses are obtained:

$$\begin{aligned}
d_{xx} &= \dot{\lambda}\left(\frac{2\sigma_{xx} - \sigma_{yy}}{\bar{\sigma}^2} + \frac{q_1 q_2 f^*}{\bar{\sigma}}\sinh\left(\frac{q_2(\sigma_{xx}^{avg} + \sigma_{yy}^{avg} + \sigma_{zz}^{avg})}{2\bar{\sigma}}\right)\right)\\
d_{yy} &= \dot{\lambda}\left(\frac{2\sigma_{yy} - \sigma_{xx}}{\bar{\sigma}^2} + \frac{q_1 q_2 f^*}{\bar{\sigma}}\sinh\left(\frac{q_2(\sigma_{xx}^{avg} + \sigma_{yy}^{avg} + \sigma_{zz}^{avg})}{2\bar{\sigma}}\right)\right)\\
d_{zz} &= \dot{\lambda}\left(-\frac{\sigma_{xx} + \sigma_{yy}}{\bar{\sigma}^2} + \frac{q_1 q_2 f^*}{\bar{\sigma}}\sinh\left(\frac{q_2(\sigma_{xx}^{avg} + \sigma_{yy}^{avg} + \sigma_{zz}^{avg})}{2\bar{\sigma}}\right)\right)
\end{aligned} \tag{14}$$

where $\dot{\lambda}$ is the plastic flow proportionality factor.

The evolution of the void volume fraction is defined as:

$$\dot{f} = (1 - f)\,\dot{\lambda}\frac{3q_1q_2f^*}{\bar{\sigma}}\sinh\left(\frac{q_2(\sigma_{xx}^{avg} + \sigma_{yy}^{avg} + \sigma_{zz}^{avg})}{2\bar{\sigma}}\right) \tag{15}$$

where the matrix material has been assumed to be incompressible.

The momentum balance equations in the loading directions take the form:

$$\begin{aligned} F_{yy}\frac{\partial\left(h\sigma_{xx}^{avg}\right)}{\partial X} &= \rho h^0\frac{\partial V_x}{\partial t} \\ F_{xx}\frac{\partial\left(h\sigma_{yy}\right)}{\partial Y} &= \rho h^0\frac{\partial V_y}{\partial t} \end{aligned} \tag{16}$$

Note that the momentum balance equation in the out of plane direction has been disregarded, see Zaera et al. (2015) and N'souglo et al. (2021).

The solution of the problem at any given loading time, before necking localization, is called homogeneous or fundamental solution $\mathbb{S}^1 = (V_x^1, V_y^1, d_{xx}^1, d_{yy}^1, d_{zz}^1, F_{xx}^1, F_{yy}^1, F_{zz}^1, h^1, \dot{\bar{\varepsilon}}^1, \bar{\varepsilon}^1, \bar{\sigma}^1, \dot{\lambda}^1, \sigma_{xx}^1, \sigma_{yy}^1, \sigma_{xx}^{avg,1}, \sigma_{yy}^{avg,1}, \sigma_{zz}^{avg,1}, \rho^1, f^1, \varphi^1)^T$, which is obtained by solving the system of equations (1)-(6), (8) and (10)-(16) under the following initial and boundary conditions:

$$\begin{aligned} &V_x\left(X,Y,0\right) = \dot{\varepsilon}_{xx}^0 X; \qquad &&V_y\left(X,Y,0\right) = \dot{\varepsilon}_{yy}^0 Y; \qquad &&\bar{\varepsilon}\left(X,Y,0\right) = 0 \\ &h\left(X,Y,0\right) = h^0; &&f\left(X,Y,0\right) = f^0; &&\rho\left(X,Y,0\right) = \rho^0 \end{aligned}$$

$$\begin{aligned} V_x\left(L^0/2,Y,t\right) = -V_x\left(-L^0/2,Y,t\right) = \dot{\varepsilon}_{xx}^0 L^0/2 \\ V_y\left(X,L^0/2,t\right) = -V_y\left(X,-L^0/2,t\right) = \dot{\varepsilon}_{yy}^0 L^0/2 \end{aligned}$$

where $\dot{\varepsilon}_{xx}^0$ and $\dot{\varepsilon}_{yy}^0$ define the initial strain rates in X and Y directions, respectively. Hereinafter, $\dot{\varepsilon}_{xx}^0$ will be also referred to as imposed initial major strain rate. Note that the applied loading is selected through input values of $\dot{\varepsilon}_{xx}^0$ and $\chi = \dot{\varepsilon}_{yy}^0/\dot{\varepsilon}_{xx}^0$, where the ratio χ will be hereinafter referred to as loading path ($\chi = 0$ corresponds to plane strain tension, and $\chi = 1$ to equibiaxial tension).

2.2. Linear stability analysis

At some time t^1, we superimpose a small perturbation $\delta\mathbb{S}(X,t)_{t^1} = \delta\mathbb{S}^1 e^{i\xi X+\eta(t-t^1)}$ to the fundamental solution, where $\delta\mathbb{S}^1 = (\delta V_x, \delta V_y, \delta d_{xx}, \delta d_{yy}, \delta d_{zz}, \delta F_{xx}, \delta F_{yy}, \delta F_{zz}, \delta h, \delta\dot{\bar{\varepsilon}}, \delta\bar{\varepsilon}, \delta\bar{\sigma}, \delta\dot{\lambda}, \delta\sigma_{xx}, \delta\sigma_{yy}, \delta\sigma_{xx}^{avg}, \delta\sigma_{yy}^{avg}, \delta\sigma_{zz}^{avg}, \delta\rho, \delta f, \delta\varphi)^T$ is the perturbation amplitude, ξ is the wavenumber and η is the instantaneous growth rate of the perturbation at time t^1. While η and ξ are considered time independent (frozen coefficients method) for the sake of simplicity, it has to be noted that a time dependent numerical solution for the linear perturbation analysis has been recently developed by Xavier et al. (2020, 2021) for von Mises materials subjected to plane strain tension. Moreover, note that the perturbation is inserted perpendicular to the main loading direction, i.e. on lines $X = constant$, because this is the preferential orientation for an isotropic material to trigger a neck within the range of loading paths considered $0 \leq \chi < 1$, see Zaera et al. (2015) and Jacques (2020). The perturbed solution of the problem is $\mathbb{S} = \mathbb{S}^1 + \delta\mathbb{S}$, with $|\delta\mathbb{S}| \ll |\mathbb{S}^1|$, so that keeping only the first-order terms in the increments $\delta\mathbb{S}^1$, equations (1)-(6), (8) and (10)-(16) are linearized are follows:

$$\begin{aligned} &\hat{F}^1_{xx}\delta\hat{d}_{xx} + \hat{d}^1_{xx}\delta\hat{F}_{xx} - i\hat{\xi}\delta\hat{V}_x = 0 \\ &\hat{F}^1_{yy}\delta\hat{d}_{yy} + \hat{d}^1_{yy}\delta\hat{F}_{yy} = 0 \end{aligned} \tag{17}$$

$$\begin{aligned} &\left(\hat{\eta} - \hat{d}^1_{xx}\right)\delta\hat{F}_{xx} - \hat{F}^1_{xx}\delta\hat{d}_{xx} = 0 \\ &\left(\hat{\eta} - \hat{d}^1_{yy}\right)\delta\hat{F}_{yy} - \hat{F}^1_{yy}\delta\hat{d}_{yy} = 0 \end{aligned} \tag{18}$$

$$\delta\hat{h} - \delta\hat{F}_{zz} = 0 \tag{19}$$

$$\frac{1}{\hat{F}^1_{xx}}\delta\hat{F}_{xx} + \frac{1}{\hat{F}^1_{yy}}\delta\hat{F}_{yy} + \frac{1}{\hat{F}^1_{zz}}\delta\hat{F}_{zz} - \frac{1}{1-\hat{f}^1}\delta\hat{f} = 0 \tag{20}$$

$$\delta\hat{\rho} + \frac{1}{1-f^0}\delta\hat{f} = 0 \tag{21}$$

$$\hat{Q}_1\delta\hat{\sigma}^{avg}_{xx} + \hat{Q}_2\delta\hat{\sigma}^{avg}_{yy} + \hat{Q}_3\delta\hat{\sigma}^{avg}_{zz} + \hat{Q}_4\delta\hat{\sigma}_{xx} + \hat{Q}_5\delta\hat{\sigma}_{yy} + \hat{Q}_6\delta\hat{\bar{\sigma}} + \hat{Q}_7\delta\hat{f} = 0 \tag{22}$$

$$\begin{aligned}
&\delta\hat{\sigma}^{avg}_{xx} - \delta\hat{\sigma}_{xx} - \frac{2}{3}\hat{\sigma}^1_{xx}\delta\hat{\varphi} = 0 \\
&\delta\hat{\sigma}^{avg}_{yy} - \delta\hat{\sigma}_{yy} - \delta\hat{\sigma}^{avg}_{xx} + \delta\hat{\sigma}_{xx} = 0 \\
&\delta\hat{\sigma}^{avg}_{zz} - \delta\hat{\sigma}^{avg}_{xx} + \delta\hat{\sigma}_{xx} = 0
\end{aligned} \tag{23}$$

$$8\left(\hat{F}^1_{xx}\right)^2\delta\hat{\varphi} + \hat{h}^1\left(\hat{\xi}\right)^2\delta\hat{h} = 0 \tag{24}$$

$$\delta\hat{\bar{\sigma}} - \hat{P}_1\delta\hat{\bar{\varepsilon}} - \hat{P}_2\delta\hat{\dot{\bar{\varepsilon}}} = 0 \tag{25}$$

$$\delta\hat{\dot{\bar{\varepsilon}}} - \hat{\eta}\delta\hat{\bar{\varepsilon}} = 0 \tag{26}$$

$$\hat{\sigma}^1_{xx}\delta\hat{d}_{xx} + \hat{d}^1_{xx}\delta\hat{\sigma}^{avg}_{xx} + \hat{\sigma}^1_{yy}\delta\hat{d}_{yy} + \hat{d}^1_{yy}\delta\hat{\sigma}^{avg}_{yy} + \hat{d}^1_{zz}\delta\hat{\sigma}^{avg}_{zz} - \left(1-\hat{f}^1\right)\delta\hat{\bar{\sigma}} - \left(1-\hat{f}^1\right)\hat{\bar{\sigma}}^1\delta\hat{\dot{\bar{\varepsilon}}} + \hat{\bar{\sigma}}^1\delta\hat{f} = 0 \tag{27}$$

$$\begin{aligned}
&\delta\hat{d}_{xx} - \frac{\hat{d}^1_{xx}}{\hat{\dot{\lambda}}^1}\delta\hat{\dot{\lambda}} - \hat{M}_1\delta\hat{\sigma}^{avg}_{xx} - \hat{M}_2\delta\hat{\sigma}^{avg}_{yy} - \hat{M}_3\delta\hat{\sigma}^{avg}_{zz} - \hat{M}_4\delta\hat{\sigma}_{xx} - \hat{M}_5\delta\hat{\sigma}_{yy} - \hat{M}_6\delta\hat{\bar{\sigma}} - \hat{M}_7\delta\hat{f} = 0 \\
&\delta\hat{d}_{yy} - \frac{\hat{d}^1_{yy}}{\hat{\dot{\lambda}}^1}\delta\hat{\dot{\lambda}} - \hat{R}_1\delta\hat{\sigma}^{avg}_{xx} - \hat{R}_2\delta\hat{\sigma}^{avg}_{yy} - \hat{R}_3\delta\hat{\sigma}^{avg}_{zz} - \hat{R}_4\delta\hat{\sigma}_{xx} - \hat{R}_5\delta\hat{\sigma}_{yy} - \hat{R}_6\delta\hat{\bar{\sigma}} - \hat{R}_7\delta\hat{f} = 0 \\
&\delta\hat{d}_{zz} - \frac{\hat{d}^1_{zz}}{\hat{\dot{\lambda}}^1}\delta\hat{\dot{\lambda}} - \hat{S}_1\delta\hat{\sigma}^{avg}_{xx} - \hat{S}_2\delta\hat{\sigma}^{avg}_{yy} - \hat{S}_3\delta\hat{\sigma}^{avg}_{zz} - \hat{S}_4\delta\hat{\sigma}_{xx} - \hat{S}_5\delta\hat{\sigma}_{yy} - \hat{S}_6\delta\hat{\bar{\sigma}} - \hat{S}_7\delta\hat{f} = 0
\end{aligned} \tag{28}$$

$$\left(\hat{\eta}-\hat{T}_5\right)\delta\hat{f}-\frac{\hat{\dot{f}}^1}{\hat{\dot{\lambda}}^1}\delta\hat{\dot{\lambda}}-\hat{T}_1\delta\hat{\sigma}_{xx}^{avg}-\hat{T}_2\delta\hat{\sigma}_{yy}^{avg}-\hat{T}_3\delta\hat{\sigma}_{zz}^{avg}-\hat{T}_4\delta\hat{\bar{\sigma}}=0 \tag{29}$$

$$\begin{aligned}&i\hat{\xi}\hat{F}_{yy}^1\hat{\sigma}_{xx}^1\delta\hat{h}+i\hat{\xi}\hat{h}^1\hat{F}_{yy}^1\delta\hat{\sigma}_{xx}^{avg}-\frac{1}{\tilde{L}^2}\hat{\rho}^1\hat{\eta}\delta\hat{V}_x=0\\&\delta\hat{V}_y=0\end{aligned} \tag{30}$$

This system of equations has been adimensionalized by introducing the following dimensionless groups:

$$\begin{aligned}
&\hat{V}_x=\frac{V_x}{h^0\dot{\bar{\varepsilon}}^1};\quad \hat{V}_y=\frac{V_y}{h^0\dot{\bar{\varepsilon}}^1};\quad \hat{d}_{xx}=\frac{d_{xx}}{\dot{\bar{\varepsilon}}^1};\quad \hat{d}_{yy}=\frac{d_{yy}}{\dot{\bar{\varepsilon}}^1};\quad \hat{d}_{zz}=\frac{d_{zz}}{\dot{\bar{\varepsilon}}^1};\quad \hat{F}_{xx}=F_{xx};\quad \hat{F}_{yy}=F_{yy}\\
&\hat{F}_{zz}=F_{zz};\quad \hat{h}=\frac{h}{h^0};\quad \hat{\dot{\bar{\varepsilon}}}=\frac{\dot{\bar{\varepsilon}}}{\dot{\bar{\varepsilon}}^1};\quad \hat{\bar{\varepsilon}}=\bar{\varepsilon};\quad \hat{\bar{\sigma}}=\frac{\bar{\sigma}}{\sigma^0};\quad \hat{\dot{\lambda}}=\frac{\dot{\lambda}}{\sigma^0\dot{\bar{\varepsilon}}^1};\quad \hat{\sigma}_{xx}=\frac{\sigma_{xx}}{\sigma^0}\\
&\hat{\sigma}_{yy}=\frac{\sigma_{yy}}{\sigma^0};\quad \hat{\sigma}_{xx}^{avg}=\frac{\sigma_{xx}^{avg}}{\sigma^0};\quad \hat{\sigma}_{yy}^{avg}=\frac{\sigma_{yy}^{avg}}{\sigma^0};\quad \hat{\sigma}_{zz}^{avg}=\frac{\sigma_{zz}^{avg}}{\sigma^0};\quad \hat{\rho}=\frac{\rho}{\rho^0};\quad \hat{f}=f;\quad \hat{\varphi}=\varphi\\
&\hat{\eta}=\frac{\eta}{\dot{\bar{\varepsilon}}^1};\quad \hat{\xi}=\xi h^0;\quad \hat{P}_1=\frac{1}{\sigma^0}\frac{\partial\bar{\sigma}}{\partial\bar{\varepsilon}}\bigg|_{t^1};\quad \hat{P}_2=\frac{\dot{\bar{\varepsilon}}^1}{\sigma^0}\frac{\partial\bar{\sigma}}{\partial\dot{\bar{\varepsilon}}}\bigg|_{t^1};\quad \hat{Q}_1=\sigma^0\frac{\partial\Phi}{\partial\sigma_{xx}^{avg}}\bigg|_{t^1}=\hat{Q}_2=\hat{Q}_3\\
&\hat{Q}_4=\sigma^0\frac{\partial\Phi}{\partial\sigma_{xx}}\bigg|_{t^1};\quad \hat{Q}_5=\sigma^0\frac{\partial\Phi}{\partial\sigma_{yy}}\bigg|_{t^1};\quad \hat{Q}_6=\sigma^0\frac{\partial\Phi}{\partial\bar{\sigma}}\bigg|_{t^1};\quad \hat{Q}_7=\frac{\partial\Phi}{\partial f}\bigg|_{t^1}\\
&\hat{M}_1=\frac{\sigma^0}{\dot{\bar{\varepsilon}}^1}\frac{\partial d_{xx}}{\partial\sigma_{xx}^{avg}}\bigg|_{t^1}=\hat{M}_2=\hat{M}_3=\hat{R}_1=\hat{R}_2=\hat{R}_3=\hat{S}_1=\hat{S}_2=\hat{S}_3;\quad \hat{M}_4=\frac{\sigma^0}{\dot{\bar{\varepsilon}}^1}\frac{\partial d_{xx}}{\partial\sigma_{xx}}\bigg|_{t^1}=\hat{R}_5\\
&\hat{M}_5=\frac{\sigma^0}{\dot{\bar{\varepsilon}}^1}\frac{\partial d_{xx}}{\partial\sigma_{yy}}\bigg|_{t^1}=\hat{R}_4=\hat{S}_4=\hat{S}_5;\quad \hat{M}_6=\frac{\sigma^0}{\dot{\bar{\varepsilon}}^1}\frac{\partial d_{xx}}{\partial\bar{\sigma}}\bigg|_{t^1};\quad \hat{M}_7=\frac{1}{\dot{\bar{\varepsilon}}^1}\frac{\partial d_{xx}}{\partial f}\bigg|_{t^1}=\hat{R}_7=\hat{S}_7\\
&\hat{R}_6=\frac{\sigma^0}{\dot{\bar{\varepsilon}}^1}\frac{\partial d_{yy}}{\partial\bar{\sigma}}\bigg|_{t^1};\quad \hat{S}_6=\frac{\sigma^0}{\dot{\bar{\varepsilon}}^1}\frac{\partial d_{zz}}{\partial\bar{\sigma}}\bigg|_{t^1};\quad \hat{\dot{f}}^1=\frac{\dot{f}^1}{\dot{\bar{\varepsilon}}^1};\quad \hat{T}_1=\frac{\sigma^0}{\dot{\bar{\varepsilon}}^1}\frac{\partial\dot{f}}{\partial\sigma_{xx}^{avg}}\bigg|_{t^1}=\hat{T}_2=\hat{T}_3\\
&\hat{T}_4=\frac{\sigma^0}{\dot{\bar{\varepsilon}}^1}\frac{\partial\dot{f}}{\partial\bar{\sigma}}\bigg|_{t^1};\quad \hat{T}_5=\frac{1}{\dot{\bar{\varepsilon}}^1}\frac{\partial\dot{f}}{\partial f}\bigg|_{t^1};\quad \frac{1}{\tilde{L}^2}=\frac{\rho^0\left(h^0\dot{\bar{\varepsilon}}^1\right)^2}{\sigma^0}
\end{aligned}$$

A non-trivial solution for $\delta\hat{\mathbb{S}}^1$ is obtained by imposing that the determinant of the matrix of coefficients of the system of linear algebraic equations (17)-(30) is equal to zero, which leads to a fourth order polynomial for $\hat{\eta}$ which depends on the adimensionalized fundamental solution $\hat{\mathbb{S}}^1$ and on the adimensionalized wavenumber $\hat{\xi}$. The adimensionalized wavenumber is related to the normalized perturbation wavelength as $L^0/h^0=2\pi\hat{\xi}^{-1}$ (see N'souglo et al. (2020, 2021)). Note that the normalized perturbation wavelength is usually referred to as necking wavelength (N'souglo et al., 2020; Rodríguez-Martínez et al., 2021). The root of the polynomial with physical meaning is the one with the greatest positive real part (Dudzinski and Molinari, 1991), hereinafter denoted by $\hat{\eta}^+$. According to the notation used by El Maï et al. (2014) and Rodríguez-Martínez et al. (2021), among others, $\hat{\eta}^+$ will be referred to as instantaneous instability index, and it will be used to compute the so-called cumulative instability index $I = \int_0^t \hat{\eta}^+ \dot{\bar{\varepsilon}}^1 \mathrm{d}\tau$, which tracks the history of the instantaneous grow rate of all the growing modes. The cumulative instability index generally provides better predictions than the instantaneous instability index for the critical strain leading to necking formation at high strain rates (see the recent paper of Rodríguez-Martínez et al. (2021)). Assuming that a perturbation mode turns into a necking mode when the cumulative instability index reaches a critical value which depends on the loading path and the strain rate, see Section 3.1, the linear stability analysis is used in Section 3 to construct forming limit diagrams which are compared with unit-cell finite element simulations performed in ABAQUS/Explicit (2019) to demonstrate the ability of the analytical model to capture the effect of porosity on necking localization (this is same methodology used by N'souglo et al. (2021) to assess the ability of the linear stability analysis to capture the effect of anisotropy on necking localization in materials described with Hill (1948) yield criterion). Details of the unit-cell finite element model –which is not shown here for the sake of brevity– can be found in Sections 4.1 and 5 of Rodríguez-Martínez et al. (2017) and N'souglo et al. (2021), respectively. In the finite element calculations, the flow strength of the matrix material, equation (11), has been used along with the Gurson-Tvergaard-Needleman model pre-implemented in ABAQUS/Explicit through a user-defined subroutine VUHARD (ABAQUS/Explicit, 2019).

The linear stability analysis has been implemented in the software Wolfram Mathematica. In *Supplementary material*, we include the links to download all the codes developed, which come with specific instructions for reproducing the stability analysis results reported in Section 3.

3. Results

This section of the paper is split into three parts. In Section 3.1, we show the procedure for calibration of the linear stability analysis using unit-cell finite element calculations. Moreover, the effect of initial void volume fraction on the critical strain leading to necking formation is investigated in Section 3.2, while the effect of loading rate is explored in Section 3.3. Results are presented for loading paths ranging from plane strain tension ($\chi = 0$) to nearly equibiaxial tension, for imposed initial major strain rates varying between 100 s^{-1} and 10000 s^{-1}, and for different initial void volume fractions spanning from 0.01 to 0.1. For all the calculations performed, the initial thickness of the plate is $h^0 = 2$ mm. In the unit-cell finite element simulations, the normalized imperfection amplitude is $\Delta = 0.2\%$ (see Section 5 of N'souglo et al. (2021)). The baseline numerical values of the material parameters employed in the stability analysis and in the finite element simulations are given in Table 1. We use standard values representative of general purpose steel. Note that in some calculations presented in Sections 3.2 and 3.3 we disregard voids coalescence and fracture considering that $f_c \rightarrow \infty$ and $f_f \rightarrow \infty$. Note also that, unlike the stability analysis, the finite element calculations performed for comparison with the analytical model predictions consider the elastic response of the material, which is assumed to be isotropic and linear.

Symbol	**Property and units**	**Value**
ρ^0	Initial density (kg/m^3)	7850
G	Elastic shear modulus (GPa)	75.19
K	Bulk modulus (GPa)	196.1
q_1	Material parameter, Eq. (6)	1.25
q_2	Material parameter, Eq. (6)	1
f_c	Material parameter, Eq. (7)	red 0.12
f_f	Material parameter, Eq. (7)	0.5
σ^0	Material parameter (MPa), Eq. (11)	300
ε^0	Material parameter, Eq. (11)	0.023
n	Material parameter, Eq. (11)	0.12
m	Material parameter, Eq. (11)	0.01
$\dot{\varepsilon}^0$	Material parameter (s^{-1}), Eq. (11)	1000

Table 1: *Baseline numerical values of the material parameters employed in the stability analysis and in the finite element simulations. The values of the parameters corresponding to the flow strength of the matrix material are taken from N'souglo et al. (2021).*

3.1. Calibration of the linear stability analysis

We have enhanced the procedure developed by N'souglo et al. (2020) to calibrate the linear stability analysis so that in this paper a perturbation mode is assumed to turn into a necking mode when the cumulative instability index reaches a critical value which depends on the imposed initial major strain rate and on the loading path (recall that N'souglo et al. (2020, 2021) assumed I^c to be constant):

$$I^c\left(\dot{\varepsilon}^0_{xx}, \chi\right) = a + b\chi + c\dot{\varepsilon}^0_{xx} + d\chi^2 + e(\dot{\varepsilon}^0_{xx})^2 \tag{31}$$

where a, b, c, d and e are calibration coefficients to be determined. For that purpose, we have devised a two-steps methodology in which the results of the stability analysis for the evolution of the major necking strain ε^{neck}_{xx} with the necking wavelength L^0/h^0 are fitted to unit-cell calculations for different cell lengths in which the material behaviour is modelled with von Mises plasticity (i.e. imposing $f^0 = 0$ on the Gurson-Tvergaard-Needleman constitutive relation):

1. For plane strain tension $\chi = 0$ and initial major strain rates $\dot{\varepsilon}^0_{xx} = 1000$, 5000 and 10000 s^{-1}, the best fitting between stability analysis and finite element results is obtained for $I^c = 3.8$, 4.33 and 4.9, respectively, so that $a = 3.65722$, $c = 0.000144833$ s and $e = -2.05556 \cdot 10^{-9}$ s^2 (see Fig. 2(a)).

2. For imposed initial major strain rate $\dot{\varepsilon}^0_{xx} = 10000$ s^{-1} and loading paths $\chi = 0.5$ and 0.75, the best fitting between stability analysis and finite element results is obtained for $I^c = 5.78$ and 6.19, respectively, so that $b = 1.84$ and $d = -0.16$ (see Fig. 2(b)).

The major necking strain is the logarithmic strain in the major loading direction when necking occurs and it is determined both in the stability analysis and in the finite element simulations as in N'souglo et al. (2021), so that the reader is referred to Section 6.1 therein for the procedure to obtain ε^{neck}_{xx}, and no additional details are provided here for the sake of brevity. The $\varepsilon^{neck}_{xx} - L^0/h^0$ curves display a nonlinear concave-upward shape, so that the major necking strain first decreases, reaches a minimum for an intermediate value of L^0/h^0, and then increases (the increase being less as the loading rate decreases, so that for 100 s^{-1} the minimum of the $\varepsilon^{neck}_{xx} - L^0/h^0$ curve is shallow). The larger values of the major necking strain for small and large values of L^0/h^0 are due to the stabilizing effects of stress multiaxiality and inertia, respectively (Fressengeas and Molinari, 1994; Mercier and Molinari, 2003). The minimum value of ε^{neck}_{xx}, also referred to as critical major necking strain and hereinafter denoted by ε^c_{xx}, determines the size of the necks $\left(L^0/h^0\right)^c$ which form earlier, i.e. the necks which require less energy to develop (N'souglo et al., 2020). Note that the critical major necking strain ε^c_{xx} increases as the loading path moves away from plane strain and approaches equibiaxial tension, and the value of $\left(L^0/h^0\right)^c$ decreases with the imposed initial major strain rate. Moreover, following the procedure detailed in Section 6.1 of N'souglo et al. (2021), the critical major necking strain ε^c_{xx} and the corresponding critical minor necking strain ε^c_{yy} (i.e. the logarithmic strain in the minor loading direction when necking occurs, i.e. when ε^c_{xx} is measured), obtained from the finite element calculations and the linear stability analysis for different loading paths and loading rates, are used in the following sections of this paper to construct forming limit diagrams. Namely, the predictions of the linear stability analysis obtained with the calibrated necking criterion (31) will be compared with finite element calculations in which the material is modeled with the Gurson-Tvergaard-Needleman constitutive relation (i.e. $f^0 \neq 0$). Note that, while the results of the stability analysis for the von Mises material are fitted (see Fig. 2), the results for the porous material will be predicted.

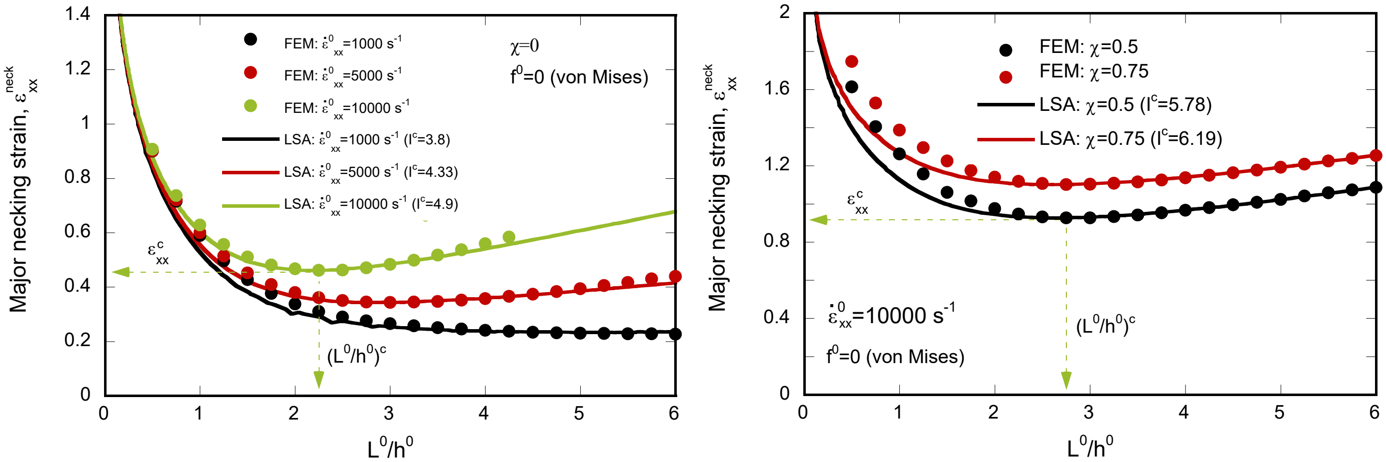

(a) (b)

Figure 2: Calibration of the linear stability analysis (LSA) with the finite element calculations (FEM). Major necking strain ε_{xx}^{neck} versus L^0/h^0 (dimensionless cell length and necking wavelength in the finite element calculations and in the linear stability analysis, respectively), for $f^0 = 0$ (von Mises). (a) Results are shown for $\chi = 0$ (plane strain tension) and three different imposed initial major strain rates $\dot{\varepsilon}_{xx}^0 = 1000$, 5000 and 10000 s^{-1}. (b) Results are shown for imposed initial major strain rate $\dot{\varepsilon}_{xx}^0 = 10000$ s^{-1} and two different loading paths $\chi = 0.5$ and 0.75.

3.2. The effect of porosity

The calculations presented in this section are performed for two different imposed initial major strain rates $\dot{\varepsilon}_{xx}^0 = 500$ s^{-1} and 10000 s^{-1}, for which the value of the inertia parameter is $\tilde{L}^{-1} \approx 0.005$ and ≈ 0.1, respectively. This range of strain rates lies within the loading conditions attained in dynamic forming processes (e.g. see Dariani et al. (2009), Golovashchenko et al. (2013) and Li et al. (2017), among others). Moreover, the numerical results reported by N'souglo et al. (2020) and Zheng et al. (2020) indicated that the effect of inertia on neck retardation starts to be important for $\tilde{L}^{-1}$ in the range $0.06 - 0.1$. Initial void volume fractions ranging from 0.01 to 0.1 are considered. This range of values of f^0 is chosen because sintered and additively manufactured metals contain residual porosities that can be as large as 10% (e.g. see Aboulkhair et al. (2014), Heidari et al. (2020) and Marvi-Mashhadi et al. (2021)). In addition, exploring a wide range of initial void volume fractions helps to enlighten the effect of porosity on necking formation for different loading paths. We have also performed calculations for $f^0 = 0$, which corresponds to von Mises (1928) plasticity (fully dense material).

Fig. 3 compares forming limit diagrams (critical major necking strain ε_{xx}^c versus critical minor necking strain ε_{yy}^c) predicted by the stability analysis with finite element calculations for two values of the initial void volume fraction: $f^0 = 0$ (von Mises) and $f^0 = 0.1$. For the porous material, void coalescence and fracture have been disregarded, i.e. $f^* = f$ considering $f_c \to \infty$ and $f_f \to \infty$, see equation (7). The imposed initial major strain rate is $\dot{\varepsilon}_{xx}^0 = 10000 \text{ s}^{-1}$. There is a monotonic increase of ε_{xx}^c as the value of χ increases so that the minimum critical major necking strain corresponds to plane strain tension ($\chi = 0$). This trend is consistent with experimental, numerical and analytical results published elsewhere (Kuroda and Tvergaard, 2000; Brunet and Morestin, 2001; Banabic et al., 2010). Moreover, as compared to the results obtained with the von Mises material, increasing the initial porosity up to 0.1 shifts the $\varepsilon_{xx}^c - \varepsilon_{yy}^c$ curve downwards. The drop of ε_{xx}^c is maximum for $\chi = 0$ ($\approx 15\%$), and decreases as the loading path approaches equibiaxial tension. Moreover, note that the agreement between the theoretical predictions and the numerical simulations is excellent for the whole range of loading paths considered. In this regard, recall that the calibration of the stability analysis, equation (31), was performed using the numerical results obtained for $\dot{\varepsilon}_{xx}^0 = 10000 \text{ s}^{-1}$ for the von Mises material, which explains the *perfect* matching between finite element calculations and stability analysis for $f^0 = 0$. On the other hand, the results of the analytical model for $f^0 = 0.1$ are *fully predictive*, i.e. none of the finite element results for this initial void volume fraction was used for the calibration of the stability analysis, so that the agreement between both approaches makes apparent the ability of the linear perturbation model to capture the effect of porosity on the necking formability of porous metals.

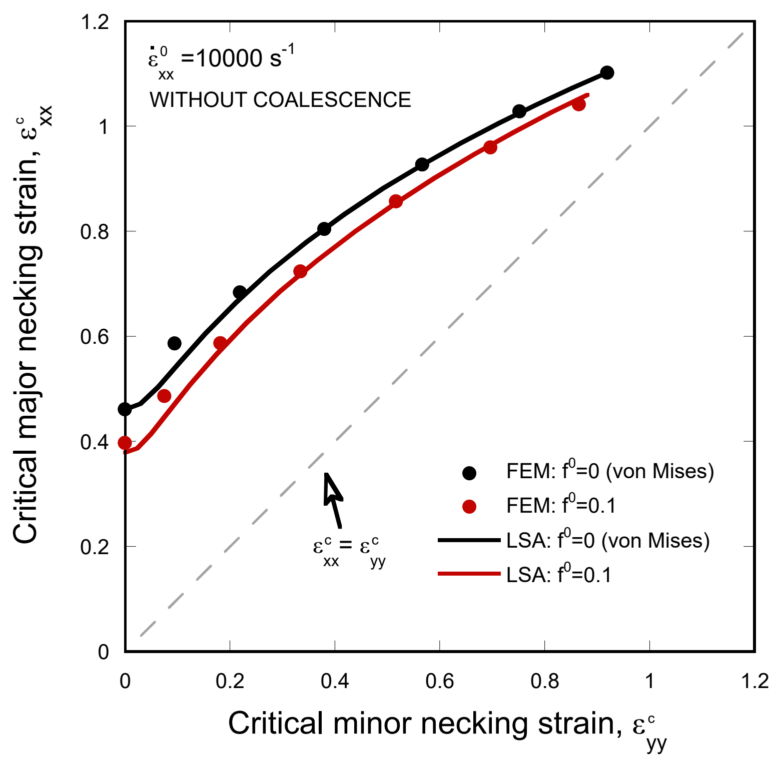

Figure 3: Comparison between finite element results (FEM) and linear stability analysis predictions (LSA). Forming limit diagrams, critical major necking strain ε_{xx}^c versus critical minor necking strain ε_{yy}^c, for loading conditions ranging from plane strain stretching ($\chi = 0$) to nearly equibiaxial tension. Results are shown for initial void volume fraction $f^0 = 0$ (von Mises) and $f^0 = 0.1$ disregarding void coalescence, i.e. $f^* = f$, see equation (7). The imposed initial major strain rate is $\dot{\varepsilon}_{xx}^0 = 10000 \text{ s}^{-1}$.

Fig. 4 illustrates the influence of void coalescence on forming limit diagrams calculated using finite element simulations and predicted with the stability analysis for three different values of the initial void volume fraction $f^0 = 0.01$, 0.02 and 0.03. Namely, Fig. 4a shows results for $f_c \to \infty$ and $f_f \to \infty$ (i.e. $f^* = f$), so that the constitutive model accounts for the growth of voids while neglecting coalescence and fracture, and Fig. 4b considers that $f_c = 0.12$ and $f_f = 0.5$ (see Table 1). We have checked that in all the calculations included in Fig. 4b necking occurs before fracture (recall that the stability analysis only models necking). As in Fig. 3, the imposed initial major strain rate is $\dot{\varepsilon}^0_{xx} = 10000$ s^{-1}. The quantitative agreement between the predictions of the analytical model and the numerical simulations is excellent for all the loading paths investigated, and for the three values of the initial void volume fraction considered. Note that, if coalescence and fracture are disregarded, Fig. 4a, the influence of the initial porosity on the forming limit diagrams, for the three values of f^0 considered, is small. For plane strain tension the critical major necking strain ε^c_{xx} is slightly smaller as the initial void volume fraction increases, while the trend is reversed near equibiaxial tension. In contrast, accounting for voids coalescence boosts the effect of initial void volume fraction on the forming limit diagrams, see Fig. 4b. Specifically, the critical major necking strain ε^c_{xx} decreases with the value of f^0 for all the loading paths investigated, and the difference between the results obtained for different values of the initial porosity increases as the loading path approaches equibiaxial tension. Note that, as the initial void volume fraction increases, less plastic deformation is needed to meet the coalescence criterion, leading to earlier drop of the flow stress, which favors necking formation, shifting downwards the $\varepsilon^c_{xx} - \varepsilon^c_{yy}$ curve. For instance, the stability analysis predicts that coalescence occurs for $\varepsilon^c_{yy} = 0.35$, 0.19 and 0.07 in the cases of $f^0 = 0.01$, 0.02 and 0.03, respectively, while the values obtained with the finite element calculations for the same initial void volume fractions are $\varepsilon^c_{yy} = 0.35$, 0.19 and 0.08.

Fig. 5 shows forming limit diagrams for lower imposed initial major strain rate $\dot{\varepsilon}^0_{xx} = 500$ s^{-1} (20 times lower than in Fig. 4). The results are qualitatively the same as those obtained for 10000 s^{-1}, and the agreement between finite element simulations and analytical predictions is excellent for all the loading paths. If coalescence and fracture are disregarded, $f_c \to \infty$ and $f_f \to \infty$, the results obtained for $f^0 = 0.01$, 0.02 and 0.03 are very similar, see Fig. 5a. Near plane strain tension the value of ε^c_{xx} is slightly smaller as f^0 increases, while this trend is reversed as the loading path approaches equibiaxial tension, as in the case of $\dot{\varepsilon}^0_{xx} = 10000$ s^{-1} shown in Fig. 4a. On the other hand, including coalescence and fracture in the calculations, $f_c = 0.12$ and $f_f = 0.5$, see Fig. 5b, yields differences in the results obtained for the three values of f^0 considered which increase as the loading path moves away from plane strain, as in the case of $\dot{\varepsilon}^0_{xx} = 10000$ s^{-1} shown in Fig. 4b. Moreover, note that the main quantitative difference between the forming limit diagrams obtained for 10000 s^{-1} and 500 s^{-1} is that,

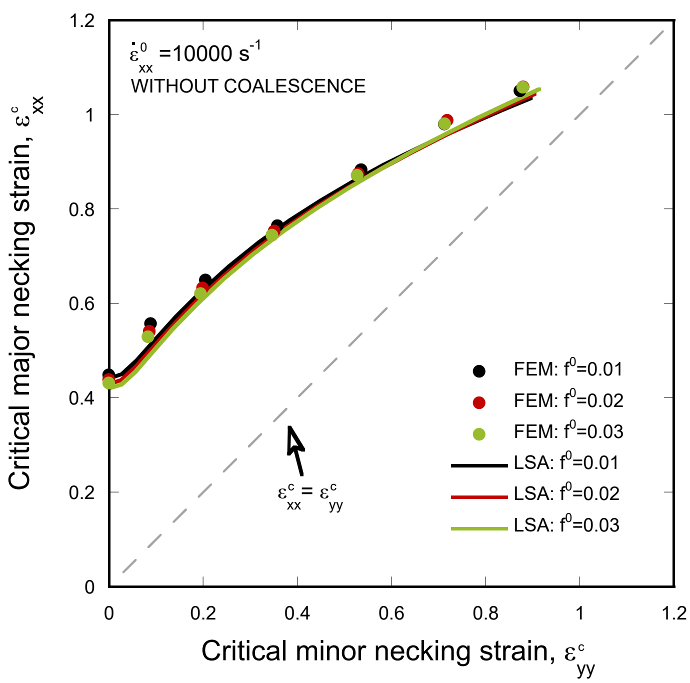

(a)

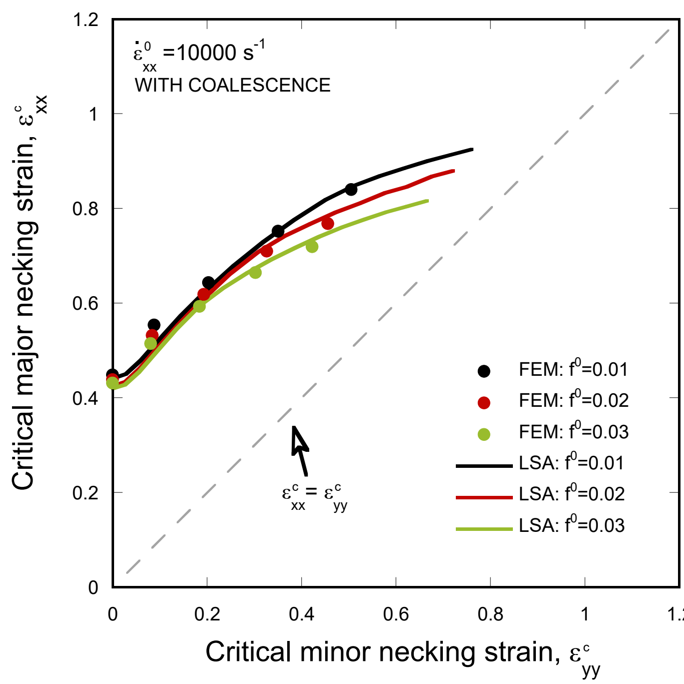

(b)

Figure 4: Comparison between finite element results (FEM) and linear stability analysis predictions (LSA). Forming limit diagrams, critical major necking strain ε^c_{xx} versus critical minor necking strain ε^c_{yy}, for loading conditions ranging from plane strain stretching ($\chi = 0$) to nearly equibiaxial tension. Results are shown for three values of the initial void volume fraction $f^0 = 0.01$, 0.02 and 0.03. The imposed initial major strain rate is $\dot{\varepsilon}^0_{xx} = 10000$ s^{-1}. Results corresponding to: (a) $f_c \to \infty$ and $f_f \to \infty$ (i.e. $f^* = f$), so that the constitutive model accounts for the growth of voids while neglecting coalescence and fracture, and (b) $f_c = 0.12$ and $f_f = 0.5$ (see Table 1).

independently of the value of the initial void volume fraction, increasing the loading rate shifts the $\varepsilon^c_{xx} - \varepsilon^c_{yy}$ curves upwards due to the stabilizing effect of inertia which delays necking formation (we further elaborate on this issue in Section 3.3).

These results highlight the influence of void coalescence in the formability limits of porous metals, and reinforce the idea that the stability analysis captures the mechanisms controlling the formation of dynamic necks for different loading paths, loading rates and void volume fractions.

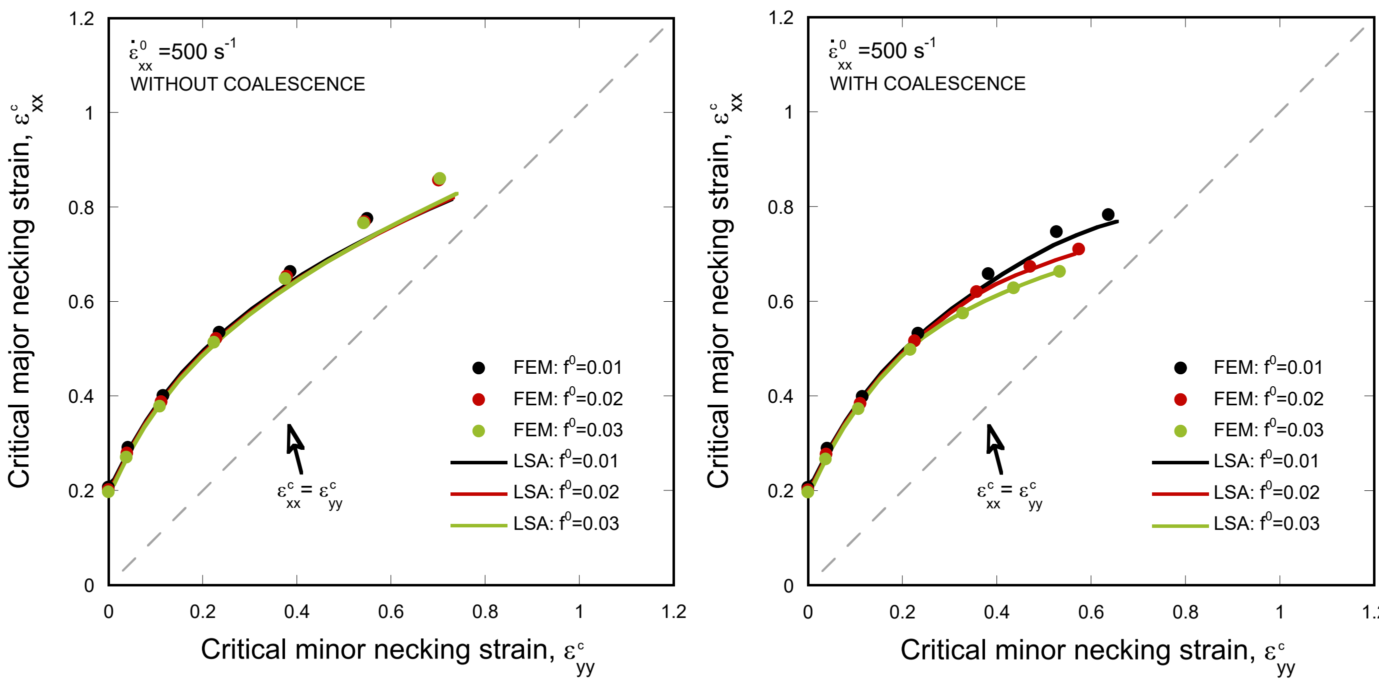

(a) (b)

Figure 5: Comparison between finite element results (FEM) and linear stability analysis predictions (LSA). Forming limit diagrams, critical major necking strain ε^c_{xx} versus critical minor necking strain ε^c_{yy}, for loading conditions ranging from plane strain stretching ($\chi = 0$) to nearly equibiaxial tension. Results are shown for three values of the initial void volume fraction $f^0 = 0.01$, 0.02 and 0.03. The imposed initial major strain rate is $\dot{\varepsilon}^0_{xx} = 500$ s^{-1}. Results corresponding to: (a) $f_c \to \infty$ and $f_f \to \infty$ (i.e. $f^* = f$), so that the constitutive model accounts for the growth of voids while neglecting coalescence and fracture, and (b) $f_c = 0.12$ and $f_f = 0.5$ (see Table 1).

3.3. The effect of loading rate

The calculations presented in this section are performed for imposed initial major strain rates ranging from 100 s^{-1} to 10000 s^{-1}, and for three different values of the initial void volume fraction $f^0 = 0.01$, 0.02 and 0.03.

Fig. 6 compares forming limit diagrams calculated using finite element simulations and predicted by the stability analysis for four different values of the imposed initial major strain rate: 500 s^{-1}, 2000 s^{-1}, 5000 s^{-1} and 10000 s^{-1}. The initial void volume fraction is $f^0 = 0.01$. Results disregarding voids coalescence and fracture are shown in Fig. 6a. The theoretical predictions are in excellent accord with the numerical results. As anticipated in previous section, the stabilizing effect of inertia enhances the formability of the material as the strain rate increases. Notice that the gap between the curves obtained for different strain rates is roughly constant for all the loading paths considered, showing that the relative contribution of inertia to neck retardation decreases as the loading path moves away from plane strain and approaches equibiaxial tension, in agreement with the finite element simulations performed by N'souglo et al. (2021) for anisotropic materials modelled with Hill (1948) criterion. Results considering voids coalescence and fracture are shown in Fig. 6b. We have checked that necking occurs before fracture (recall that the stability analysis only models necking). As in Fig. 6a, the gap between the curves obtained for different strain rates is very similar for all loading paths. Note that the difference with the results reported in Fig. 6a for the simulations with $f^* = f$ is that the formability of the material is reduced near equibiaxial tension (therefore the relative influence of coalescence on the formability is more as equibiaxial tension is approached). The stability analysis predicts that coalescence occurs for $\varepsilon^c_{yy} = 0.35$, 0.38, 0.43 and 0.51, in the cases of $\dot{\varepsilon}^0_{xx} = 500$ s^{-1}, 2000 s^{-1}, 5000 s^{-1} and 10000 s^{-1}, respectively, while the values obtained with the finite element simulations are $\varepsilon^c_{yy} = 0.38$, 0.40, 0.44 and 0.50. These results show that increasing the loading rate delays the onset of coalescence.

The influence of the loading rate on necking formation is further investigated in Fig. 7, which pictures the comparison between finite element simulations and linear stability analysis for the evolution of the critical major necking strain ε^c_{xx} with imposed initial major strain rate $\dot{\varepsilon}^0_{xx}$ for three different values of the initial void volume fraction $f^0 = 0.01$, 0.02 and 0.03. Note that the range of values of $\dot{\varepsilon}^0_{xx}$ considered spans two decades of strain rate. Results are shown for two different loading paths $\chi = 0$ and 0.5. The $\varepsilon^c_{xx} - \dot{\varepsilon}^0_{xx}$ curves display a concave-upward shape, showing that the increase of the necking strain with the loading rate is nonlinear, in agreement with the finite element results shown in Rodríguez-Martínez et al. (2017) and N'souglo et al. (2021) for fully dense materials modelled with von Mises (1928) and Hill (1948) yield criteria, respectively.

Results corresponding to $f_c \to \infty$ and $f_f \to \infty$ (i.e. $f^* = f$) are shown in Figs. 7a and 7b. The differences between the $\varepsilon^c_{xx} - \dot{\varepsilon}^0_{xx}$ curves obtained for different initial void volume fractions are very small, consistently with the results previously shown in Figs. 4a and 5a. The agreement between stability analysis predictions and finite element calculations is excellent for the whole range of strain rates considered in the case of $\chi = 0$, see Fig. 7a. Moreover, for the loading path $\chi = 0.5$, the stability analysis underestimates the critical major necking strain calculated with the finite element simulations for the lower strain rates investigated (underestimation of $\approx 6\%$ for

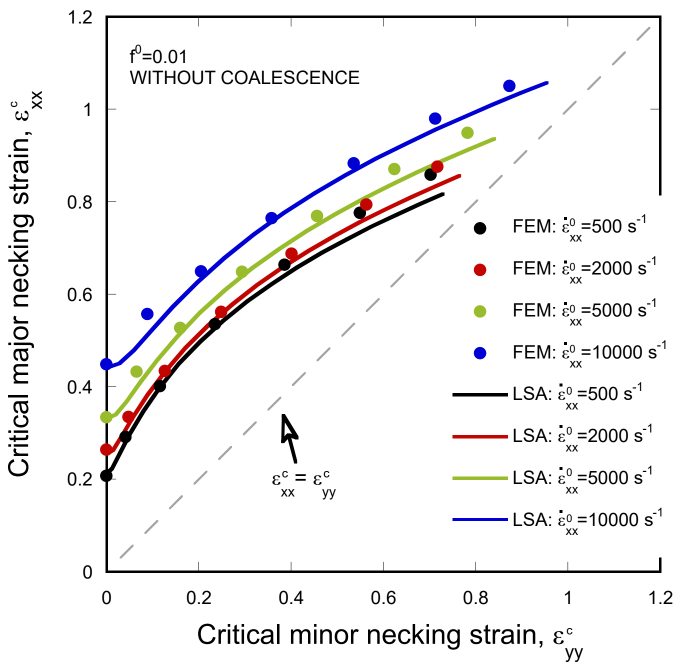

(a)

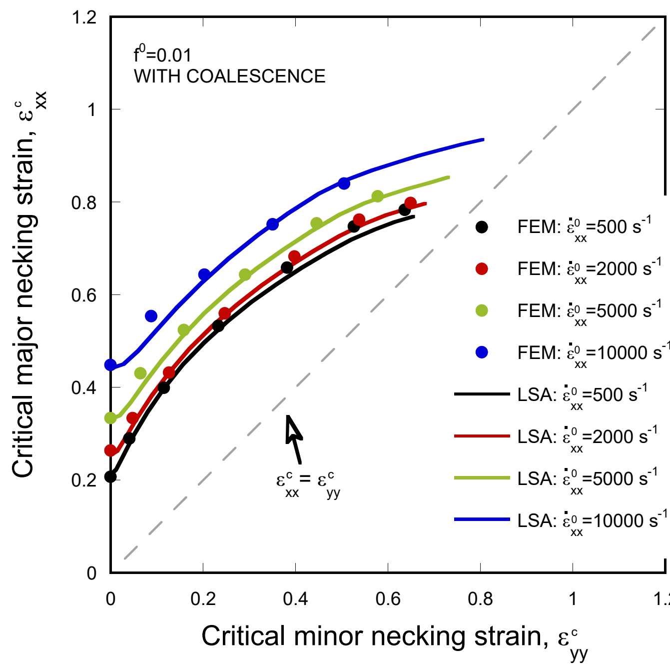

(b)

Figure 6: Comparison between finite element results (FEM) and linear stability analysis predictions (LSA). Forming limit diagrams, critical major necking strain ε^c_{xx} versus critical minor necking strain ε^c_{yy}, for loading conditions ranging from plane strain stretching ($\chi = 0$) to nearly equibiaxial tension. Results are shown for four values of the imposed initial major strain rate $\dot{\varepsilon}^0_{xx} = 500$ s^{-1}, $\dot{\varepsilon}^0_{xx} = 2000$ s^{-1}, $\dot{\varepsilon}^0_{xx} = 5000$ s^{-1} and $\dot{\varepsilon}^0_{xx} = 10000$ s^{-1}. The initial void volume fraction is $f^0 = 0.01$. Results corresponding to: (a) $f_c \to \infty$ and $f_f \to \infty$ (i.e. $f^* = f$), so that the constitutive model accounts for the growth of voids while neglecting coalescence and fracture, and (b) $f_c = 0.12$ and $f_f = 0.5$ (see Table 1).

$\dot{\varepsilon}_{xx}^0 = 100\ \mathrm{s}^{-1}$).

Results corresponding to $f_c = 0.12$ and $f_f = 0.5$ are shown in Figs. 7c and 7d. The $\varepsilon_{xx}^c - \dot{\varepsilon}_{xx}^0$ curves obtained for plane strain tension $\chi = 0$ are very similar to those obtained in Fig. 7a, showing that necking occurs before the coalescence criterion is met, for this loading path, for the whole range of strain rates considered. In contrast, for the loading path $\chi = 0.5$, there are differences between the results obtained for the three initial void volume fractions considered, so that increasing the value of f^0 shifts the $\varepsilon_{xx}^c - \dot{\varepsilon}_{xx}^0$ curves downwards. In fact, the comparison with the results obtained in Fig. 7b brings out that for $f^0 = 0.02$ and 0.03 the critical major necking strain is less when coalescence is taken into account, specially, for strain rates greater than $\approx 2000\ \mathrm{s}^{-1}$. Notice that the results obtained with both finite element calculations and linear stability analysis show the same overall trends and there is also quantitative agreement for most of the loading rates considered (the accord is particularly good at high strain rates for the three void volume fractions considered).

4. Concluding remarks

In this paper, we have developed an analytical model to predict the formation of dynamic necks in ductile plates subjected to in-plane biaxial stretching for loading paths ranging from plane strain to nearly equibiaxial tension, and loading rates varying from 100 s^{-1} to 10000 s^{-1}. The novelty with respect to other stability analysis currently available in the literature is that it takes into account the material porosity using the Gurson-Tvergaard-Needleman constitutive relation for progressively cavitating solids (Gurson, 1977; Tvergaard, 1981, 1982; Tvergaard and Needleman, 1984). The calibration of the analytical model has been performed assuming that a perturbation mode turns into a necking mode when the cumulative instability index meets a critical value that depends on the loading path and the strain rate. Excellent qualitative and quantitative agreement has been obtained between formability diagrams predicted with the stability analysis and calculated with finite element simulations for initial void volume fractions spanning from 0.01 to 0.1. Both analytical and numerical results show that the influence of porosity on necking localization increases, due to early voids coalescence, as the loading rate increases and the loading path approaches equibiaxial tension. The stability analysis derived in this paper, which stands out for its simplicity, is intended to provide practical indications on the effect of porosity on the dynamic necking formability of sheet metal products.

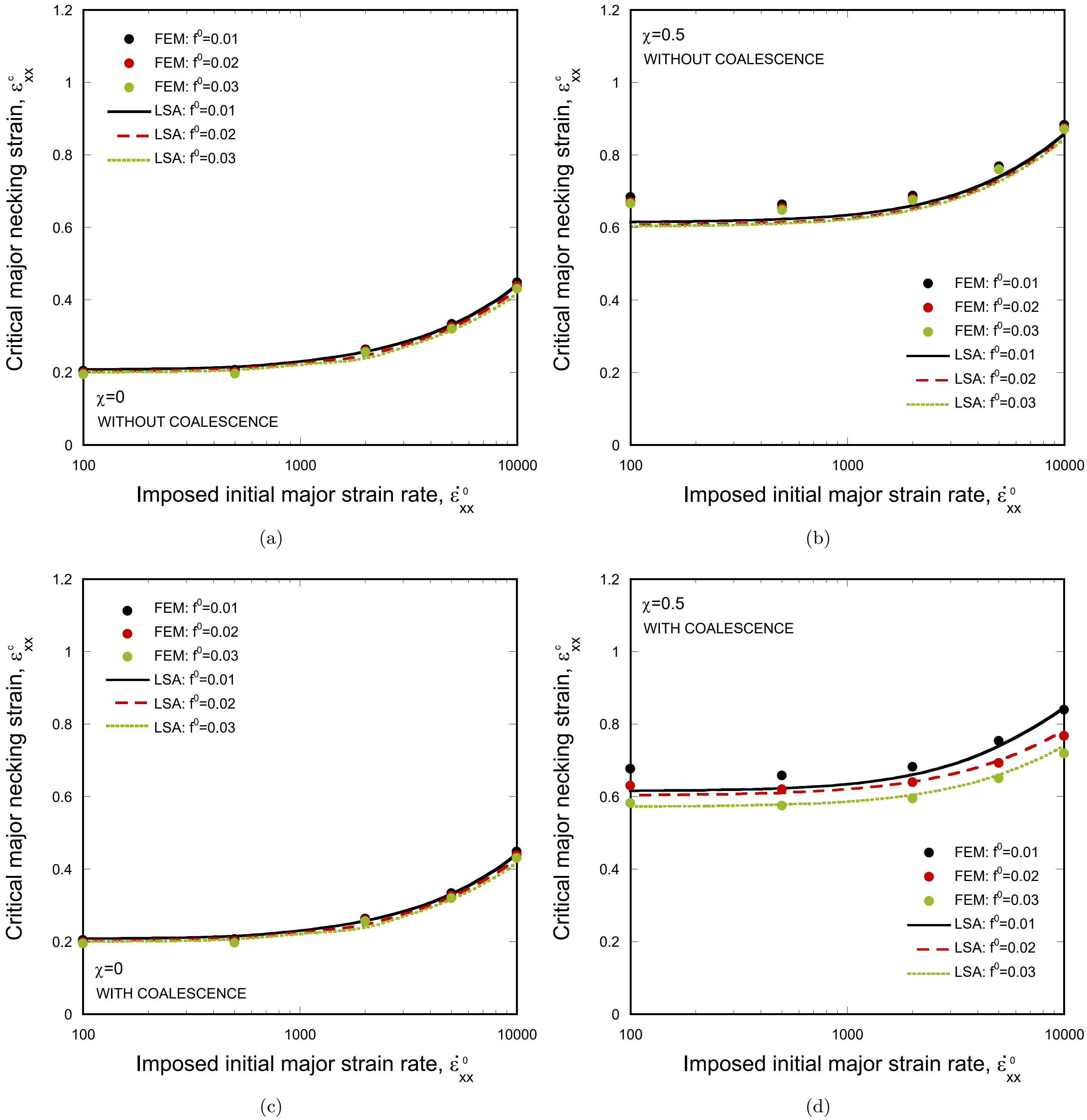

Figure 7: Comparison between finite element results (FEM) and linear stability analysis predictions (LSA). Evolution of the critical major necking strain ε^c_{xx} with imposed initial major strain rate $\dot{\varepsilon}^0_{xx}$ for three different values of the initial void volume fraction $f^0 = 0.01$, 0.02 and 0.03. Results are shown for two different loading paths: $\chi = 0$ for (a) $f_c \to \infty$ and $f_f \to \infty$ (i.e. $f^* = f$) and (c) $f_c = 0.12$ and $f_f = 0.5$, and $\chi = 0.5$ for (b) $f_c \to \infty$ and $f_f \to \infty$ (i.e. $f^* = f$) and (d) $f_c = 0.12$ and $f_f = 0.5$ (see Table 1).

Funding

The research leading to these results has received funding from the European Research Council (ERC) under the European Union's Horizon 2020 research and innovation programme. Project PURPOSE, grant agreement 758056.

Conflict of interest

The authors declare that they have no conflict of interest.

Supplementary material

In the following link we provide access the codes developed in Wolfram Mathematica to compute the stability analysis results presented in Section 3: https://doi.org/10.21950/2XVATI.

Author contributions

M. Anil Kumar: Conceptualization; Data curation; Formal analysis; Investigation; Software; Validation; Writing - original draft. **K. E. N'souglo**: Conceptualization; Data curation; Formal analysis; Investigation; Methodology; Software; Supervision; Validation; Writing - original draft; Writing - review & editing. **J. A. Rodríguez-Martínez**: Conceptualization; Formal analysis; Funding acquisition; Investigation; Methodology; Project administration; Resources; Supervision; Validation; Visualization; Roles/Writing - original draft; Writing - review & editing.

References

ABAQUS/Explicit, 2019. Abaqus Explicit v6.19 User's Manual. version 6.19 ed., ABAQUS Inc., Richmond, USA.

Aboulkhair, N.T., Everitt, N.M., Ashcroft, I., Tuck, C., 2014. Reducing porosity in AlSi10Mg parts processed by selective laser melting. Additive Manufacturing 1-4, 77 – 86. Inaugural Issue.

Altynova, M., Hu, X., Daehn, G.S., 1996. Increased ductility in high velocity electromagnetic ring expansion. Metall Trans A 27, 1837–44.

Audoly, B., Hutchinson, J.W., 2016. Analysis of necking based on a one-dimensional model. Journal of the Mechanics and Physics of Solids 97, 68 – 91. SI:Pierre Suquet Symposium.

Audoly, B., Hutchinson, J.W., 2019. One-dimensional modeling of necking in rate-dependent materials. Journal of the Mechanics and Physics of Solids 123, 149 –71. The N.A. Fleck 60th Anniversary Volume.

Banabic, D., Barlat, F., Cazacu, O., Kuwabara, T., 2010. Advances in anisotropy and formability. International Journal of Material Forming 3, 165–89.

Benzerga, A.A., Besson, J., 2001. Plastic potentials for anisotropic porous solids. European Journal of Mechanics - A/Solids 20, 397 – 434.

Bridgman, P.W., 1952. Studies in large plastic flow and fracture, with special emphasis on the effects of hydrostatic pressure, vol.1. McGraw-Hill Book Company, Inc., New York.

Brunet, M., Morestin, F., 2001. Experimental and analytical necking studies of anisotropic sheet metals. Journal of Materials Processing Technology 112, 214 –26.

Cazacu, O., Plunkett, B., Barlat, F., 2006. Orthotropic yield criterion for hexagonal closed packed metals. International Journal of Plasticity 22, 1171–94.

Chou, P.C., Carleone, J., 1977. The stability of shaped-charge jets. Journal of Applied Physics 48, 4187–95.

Considère, A., 1885. Mémoire sur l'emploi du fer et de l'acier dans les constructions. Ann. Ponts et Chaussées 9, 574–775.

Dariani, B.M., Liaghat, G.H., Gerdooei, M., 2009. Experimental investigation of sheet metal formability under various strain rates. Proceedings of the Institution of Mechanical Engineers, Part B: Journal of Engineering Manufacture 223, 703–12.

Drucker, D.C., 1949. Relation of experiments to mathematical theories of plasticity. Journal of Applied Mechanics 16, 349–57.

Dudzinski, D., Molinari, A., 1991. Perturbation analysis of thermoviscoplastic instabilities in biaxial loading. International Journal of Solids and Structures 27, 601–28.

El Maï, S., Mercier, S., Petit, J., Molinari, A., 2014. An extension of the linear stability analysis for the prediction of multiple necking during dynamic extension of round bar. International Journal of Solids and Structures 51, 3491–507.

Fressengeas, C., Molinari, A., 1985. Inertia and thermal effects on the localization of plastic flow. Acta Metallurgica 33, 387–96.

Fressengeas, C., Molinari, A., 1994. Fragmentation of rapidly stretching sheets. European Journal of Mechanics A/Solids 13, 251–68.

Gologanu, M., Leblond, J.B., Devaux, J., 1993. Approximate models for ductile metals containing non-spherical voids-case of axisymmetric prolate ellipsoidal cavities. Journal of the Mechanics and Physics of Solids 41, 1723–54.

Golovashchenko, S.F., Gillard, A.J., Mamutov, A.V., 2013. Formability of dual phase steels in electrohydraulic forming. Journal of Materials Processing Technology 213, 1191 –212.

Grady, D.E., Benson, D.A., 1983. Fragmentation of metal rings by electromagnetic loading. Experimental Mechanics 12, 393–400.

Guduru, P.R., Freund, L.B., 2002. The dynamics of multiple neck formation and fragmentation in high rate extension of ductile materials. International Journal of Solids and Structures 39, 5615–32.

Gurson, A.L., 1977. Continuum theory of ductile rupture by void nucleation and growth. Part I: Yield criteria and flow rules for porous ductile media. ASME Journal of Engineering Materials and Technology 99, 2–15.

Heidari, L., Tangestani, A., Hadianfard, M.J., Vashaee, D., Tayebi, L., 2020. Effect of fabrication method on the structure and properties of a nanostructured nickel-free stainless steel. Advanced Powder Technology 31, 3408–19.

Hill, R., 1948. A theory of the yielding and plastic flow of anisotropic metals, in: Proceedings of the Royal Society of London A: Mathematical, Physical and Engineering Sciences, The Royal Society. pp. 281–97.

Hill, R., Hutchinson, J., 1975. Bifurcation phenomena in the plane tension test. Journal of the Mechanics and Physics of Solids 23, 239–64.

Hu, X., Daehn, G.S., 1996. Effect of velocity on flow localization in tension. Acta Materialia 44, 1021–33.

Hutchinson, J.W., Neale, K.W., Needleman, A., 1978. Sheet necking-III. Strain-rate effects. Springer, Boston, MA. In Mechanics of sheet metal forming, pp. 269–85.

Jacques, N., 2020. An analytical model for necking strains in stretched plates under dynamic biaxial loading. International Journal of Solids and Structures 200-201, 198 – 212.

Jouve, D., 2013. Analytic study of plastic necking instabilities during plane tension tests. European Journal of Mechanics A/Solids 39, 180–96.

Jouve, D., 2015. Analytic study of the onset of plastic necking instabilities during biaxial tension tests on metallic plates. European Journal of Mechanics - A/Solids 50, 59–69.

Karpp, R., Simon, J., 1976. An estimate of the strength of a copper shaped charge jet and the effect of strength on the breakup of a stretching jet. US Army Ballistic Research Lab., BRL Report .

Kuroda, M., Tvergaard, V., 2000. Forming limit diagrams for anisotropic metal sheets with different yield criteria. International Journal of Solids and Structures 37, 5037–59.

Li, F., Mo, J., Li, J., Zhao, J., 2017. Formability evaluation for low conductive sheet metal by novel specimen design in electromagnetic forming. The International Journal of Advanced Manufacturing Technology 88, 1677–85.

Marvi-Mashhadi, M., Vaz-Romero, A., Sket, F., Rodríguez-Martínez, J.A., 2021. Finite element analysis to determine the role of porosity in dynamic localization and fragmentation: Application to porous microstructures obtained from additively manufactured materials. International Journal of Plasticity .

Mercier, S., Granier, N., Molinari, A., Llorca, F., Buy, F., 2010. Multiple necking during the dynamic expansion of hemispherical metallic shells, from experiments to modelling. Journal of the Mechanics and Physics of Solids 58, 955–82.

Mercier, S., Molinari, A., 2003. Predictions of bifurcations and instabilities during dynamic extensions. International Journal of Solids and Structures 40, 1995–2016.

Mises, R.V., 1928. Mechanik der plastischen formänderung von kristallen. ZAMM - Journal of Applied Mathematics and Mechanics / Zeitschrift für Angewandte Mathematik und Mechanik 8, 161–85.

Monchiet, V., Cazacu, O., Charkaluk, E., Kondo, D., 2008. Macroscopic yield criteria for plastic anisotropic materials containing spheroidal voids. International Journal of Plasticity 24, 1158–89.

N'souglo, K.E., Jacques, N., Rodríguez-Martínez, J.A., 2021. A three-pronged approach to predict the effect of plastic orthotropy on the formability of thin sheets subjected to dynamic biaxial stretching. Journal of the Mechanics and Physics of Solids 146.

N'souglo, K.E., Rodríguez-Martínez, J.A., Cazacu, O., 2020. The effect of tension-compression asymmetry on the formation of dynamic necking instabilities under plane strain stretching. International Journal of Plasticity 128.

N'souglo, K.E., Srivastava, A., Osovski, S., Rodríguez-Martínez, J.A., 2018. Random distributions of initial porosity trigger regular necking patterns at high strain rates. Proceedings of the Royal Society A: Mathematical, Physical and Engineering Sciences 474.

Rodríguez-Martínez, J.A., Cazacu, O., Chandola, N., N'souglo, K.E., 2021. Effect of the third invariant on the formation of necking instabilities in ductile plates subjected to plane strain tension. Meccanica , 1–30.

Rodríguez-Martínez, J.A., Molinari, A., Zaera, R., Vadillo, G., Fernández-Sáez, J., 2017. The critical neck spacing in ductile plates subjected to dynamic biaxial loading: on the interplay between loading path and inertia effects. International Journal of Solids and Structures 108, 74–84.

Rodríguez-Martínez, J.A., Vadillo, G., Zaera, R., Fernández-Sáez, J., Rittel, D., 2015. An analysis of microstructural and thermal softening effects in dynamic necking. Mechanics of Materials 80, 298–310. Special Issue: IUTAM Symposium on materials and interfaces under high strain rate and large deformation.

Shenoy, V., Freund, L., 1999. Necking bifurcations during high strain rate extension. Journal of the Mechanics and Physics of Solids 47, 2209–33.

Stören, S., Rice, J., 1975. Localized necking in thin sheets. Journal of the Mechanics and Physics of Solids 23, 421–41.

Tvergaard, V., 1981. Influence of voids on shear band instabilities under plane strain conditions. International Journal of Fracture 17, 389–407.

Tvergaard, V., 1982. On localization in ductile materials containing spherical voids. International Journal of Fracture 18, 237–52.

Tvergaard, V., Needleman, A., 1984. Analysis of the cup-cone fracture in a round tensile bar. Acta Metallurgica 32, 157–69.

Walsh, J., 1984. Plastic instability and particulation in stretching metal jets. Journal of Applied Physics 56, 1997–2006.

Wood, W.W., 1967. Experimental mechanics at velocity extremes - very high strain rates. Experimental Mechanics 7, 441 –6.

Xavier, M., Czarnota, C., Jouve, D., Mercier, S., Dequiedt, J.L., Molinari, A., 2020. Extension of linear stability analysis for the dynamic stretching of plates: Spatio-temporal evolution of the perturbation. European Journal of Mechanics - A/Solids 79.

Xavier, M., Mercier, S., Czarnota, C., El Mai, S., Jouve, D., Dequiedt, J.L., Molinari, A., 2021. Extension of 1D linear stability analysis based on the bridgman assumption. applications to the dynamic stretching of a plate and expansion of a ring. International Journal of Solids and Structures 217–218, 215–27.

Zaera, R., Rodríguez-Martínez, J.A., Vadillo, G., Fernández-Sáez, J., 2014. Dynamic necking in materials with strain induced martensitic transformation. Journal of the Mechanics and Physics of Solids 64, 316–37.

Zaera, R., Rodríguez-Martínez, J.A., Vadillo, G., Fernández-Sáez, J., Molinari, A., 2015. Collective behaviour and spacing of necks in ductile plates subjected to dynamic biaxial loading. Journal of the Mechanics and Physics of Solids 85, 245–69.

Zheng, X., N'souglo, K.E., Rodríguez-Martínez, J.A., Srivastava, A., 2020. Dynamics of necking and fracture in ductile porous materials. Journal of Applied Mechanics 87.

Zhou, F., Molinari, J.F., Ramesh, K.T., 2006. An elasto-visco-plastic analysis of ductile expanding ring. International Journal of Impact Engineering 33, 880–91.